Perovskite Single-Crystal Microwire-Array Photodetectors with Performance Stability beyond 1 Year

Shun-Xin Li, Yi-Shi Xu, Cheng-Long Li, Qi Guo, Gong Wang, Hong Xia,* Hong-Hua Fang, Liang Shen,* and Hong-Bo Sun*

Compared with thin-film morphology, 1D perovskite structures such as micro/nanowires with fewer grain boundaries and lower defect density are very suitable for high-performance photodetectors with higher stability. Although the stability of perovskite microwire-based photodetectors has been substantially enhanced in comparison with that of photodetectors based on thin-film morphology, practical applications require further improvements to the stability before implementation. In this study, a template-assisted method is developed to prepare methylammonium lead bromide ($MAPbBr_3$) micro/nanowire structures, which are encapsulated in situ by a protective hydrophobic molecular layer. The combination of the protective layer, high crystalline quality, and highly ordered microstructures significantly improve the stability of the $MAPbBr_3$ single-crystal microwire arrays. Consequently, these $MAPbBr_3$ single-crystal microwire-array-based photodetectors exhibit significant long-term stability, maintaining 96% of the initial photocurrent after 1 year without further encapsulation. The lifetime of such photodetectors is hence approximately four times longer than that of the most stable previously reported perovskite micro/nanowire-based photodetector; this is thought to be the most stable perovskite photodetector reported thus far. Furthermore, this work should contribute further toward the realization of perovskite 1D structures with long-term stability.

During the past decade, owing to their fascinating properties, organic–inorganic hybrid perovskite (OIHP) materials have been regarded as attractive materials for a diverse range of optoelectronic applications,[1–6] such as in solar cells,[7–11] lasers,[12–14] light-emitting diodes (LEDs),[15–17] and

S.-X. Li, Y.-S. Xu, C.-L. Li, Q. Guo, G. Wang, Prof. H. Xia, Prof. L. Shen, Prof. H.-B. Sun
State Key Laboratory of Integrated Optoelectronics
College of Electronic Science and Engineering
Jilin University
2699 Qianjin Street, Changchun 130012, China
E-mail: hxia@jlu.edu.cn; shenliang@jlu.edu.cn
Dr. H.-H. Fang, Prof. H.-B. Sun
State Key Laboratory of Precision Measurement
Technology & Instruments
Department of Precision Instrument
Tsinghua University
Haidian District, Beijing 100084, China
E-mail: hbsun@tsinghua.edu.cn

The ORCID identification number(s) for the author(s) of this article can be found under https://doi.org/10.1002/adma.202001998.

DOI: 10.1002/adma.202001998

photodetectors.[18–21] In addition to significant achievements in OIHP-based solar cells,[22–24] with increasing photo-to-electric conversion efficiency, OIHP-based photodetectors have also attracted extensive attention.[25–28] The majority of research thus far has been focused on OIHP thin-film-based photodetectors.[29–33] Despite the promising developments in OIHP thin-film-based photodetectors, their further application has been hindered by the inherent drawbacks of the OIHP thin-film morphology, such as the multitude of grain boundaries.[34,35] The presence of a large number of grain boundaries not only reduces the performance of the photodetector, but also triggers the decomposition of the perovskite, resulting from moisture and oxygen, which makes the photodetector unstable.[36–38]

1D OIHP structures, such as micro/nanowires with higher crystallization quality and fewer grain boundaries, are considered to be promising substitutions for thin films to improve the performance and stability of the OIHP-based photodetectors.[39–42] Recently, a variety of manufacturing techniques, including evaporation-induced self-assembly,[43] confinement self-assembly,[44] and template-guided self-assembly,[8] have been proposed to fabricate OIHP micro/nanowires.[45] For example, Machteld et al. achieved a $(C_6H_5CH_2NH_3)_2PbI_4$ microwire pattern with very high aspect ratios.[46] Chen et al. fabricated high-quality single-crystalline $MAPbI_3$ nanowires and created a high-performance photodetector with a long-term stability of 90 d in air.[47] Although the stability of these OIHP microwire-based photodetectors has improved compared with the thin-film morphology, their stability still requires further improvement to meet practical requirements.[35] Encapsulation is a useful method to avoid the decomposition of perovskite materials induced by oxygen and moisture, thereby improving the stability.[36] However, as a post-processing technology, the encapsulation process also inevitably prolongs the preparation period and increases the cost.[48] The passivation method, another post-processing method, also does not completely avoid water and oxygen damage.[48] Therefore, to further improve the stability of OIHP microwire-based photodetectors while minimizing preparation time and costs, it is important to develop an OIHP microwire preparation

**ADVANCED
SCIENCE NEWS**

www.advancedsciencenews.com

**ADVANCED
MATERIALS**

www.advmat.de

method that can isolate the prepared microwires from oxygen and moisture, without further encapsulation.

In this study, an in situ encapsulation method based on edge adsorption was developed to prepare MAPbBr$_3$ microwires with significantly improved stability. MAPbBr$_3$ single-crystal microwire arrays (SCMWAs) with their designable shape, controllable size, and high crystalline quality, were encapsulated in situ by a protective hydrophobic Trichloro(1H,1H,2H,2H-perfluorooctyl)silane (FOTS) molecular layer to isolate them from moisture. Additionally, the high crystalline quality of the SCMWAs effectively reduced the density of grain boundaries and defects, which play important roles in the decomposition of perovskite crystals caused by water and oxygen. Furthermore, the highly ordered microstructure of the MAPbBr$_3$ SCMWAs obtained via the proposed method improves the hydrophobicity of the surface. A lower density of grain boundaries and defects, in combination with the protective hydrophobic molecular layer, significantly improved the stability of the MAPbBr$_3$ SCMWAs. Utilizing the MAPbBr$_3$ SCMWAs, a high-performance flexible photodetector, with responsivity of 20 A W^{-1} and detectivity of 4.1×10^{11} Jones, was developed. Promisingly, the photodetectors could maintain their original performance for more than 1 year while exposed to air. The performance of the photodetector did not deteriorate even after being exposed in an environment with a relative humidity of 60% for 10 d without any encapsulation. To the authors' knowledge, this is the most stable OIHP-based photodetector by a significant margin, with the ability to be exposed to the air for long periods of time, while maintaining its initial performance. This work provides a new way to prepare high-quality perovskite micro/nanowire structures with improved intrinsic stability.

Because the inherent crystallization of the halide perovskite tends to be highly symmetric in cubic form, the crystallization kinetics needs to be strictly controlled to obtain micro/nanowire structures. An effective method of assembling perovskite molecules into a micro/nanowire structure during the solvent evaporation processes involves taking advantage of the high solubility and manipulating microdroplets or liquid films of perovskite precursor to control the crystallization process.[49] Flexible microstructured poly(dimethylsiloxane) (PDMS) templates were used to control the growth direction and position of the MAPbBr$_3$ crystal to obtain well-aligned MAPbBr$_3$ SCMWAs.[50,51] Unlike in previous reports, the PDMS template used had a layer of hydrophobic FOTS molecules on its surface. As shown in Figure S1, Supporting Information, to make the PDMS film more easily removable from the Si template, a layer of FOTS molecules was evaporated onto the Si template.[46] These hydrophobic FOTS molecules were partially transferred to the surface of the PDMS template during the fabrication process (Figure S2, Supporting Information).

The specific fabrication procedures of the MAPbBr$_3$ SCMWAs are shown in **Figure 1**. First, a PDMS template with periodic microgroove-protrusion structures (Figure S3, Supporting Information) was tightly bonded to the substrate to form a series of sealed periodic microchannels. To avoid having the PDMS template blown away from the substrate by the vaporized solvent during the solvent evaporation process, a spacer was used to pad one end of the template, forming an opening to vent the solvent vapor from the microchannels, as

shown in Figure 1a. Under the influence of the capillary force, the MAPbBr$_3$ precursor quickly flowed into these periodic microchannels after being deposited on one end of the template, as shown in Figures 1b and 1c. Under adequate heating, approximately 60 °C, the solvent gradually evaporated. Because of the sealed microchannels, the solvent evaporation process was confined within the microchannels, and the liquid could only flow along the direction of the microchannels. In addition, because of the adsorption to the sidewalls of the microchannels, there were two liquid tails attached to the sidewalls of each microchannel while the liquid flowed through the channel, forming a three-phase-contact line moving along the sidewall (Figure 1d). These tails led to preferential crystallization along the sidewalls, resulting in high-quality MAPbBr$_3$ SCMWAs, as shown in Figure 1e. After the solvent evaporation process was completed, the PDMS template and spacer were peeled off from the substrate, leaving highly aligned MAPbBr$_3$ SCMWAs on the substrate, as shown in Figure 1f. During this process, the hydrophobic FOTS molecules on the surface of PDMS microstructures were transferred to the surface of the fabricated MAPbBr$_3$ SCMWAs, forming an in situ encapsulation layer, which significantly enhanced the resistance against water and oxygen. The strong adhesion of PDMS enables the large-scale fabrication of MAPbBr$_3$ SCMWAs on a variety of substrates, such as glass, silicon, and poly(ethylene terephthalate)) (PET), as shown in Figure 1g–i.

The high crystalline quality and uniform morphology of the MAPbBr$_3$ SCMWAs obtained through this process were analyzed, as shown in **Figure 2**. Figure 2a presents the fluorescence photograph of the MAPbBr$_3$ SCMWAs excited by a 405 nm laser. The uniform green lines represent the microwires, indicating the excellent uniform crystallinity of the MAPbBr$_3$ crystals. The black portion between the green lines demonstrates that there are no excess residual layers between the microwires. The crystallinity of the MAPbBr$_3$ microwire arrays was further analyzed by X-ray diffraction (XRD). As shown in Figure S4, Supporting Information, the sharp and strong (00l) diffraction peaks indicate the orientation of the microwires. Because the MAPbBr$_3$ SCMWAs strictly adhere to the pattern of the templates, the resulting microwire arrays are as precisely aligned as the template patterns. Thus, the patterns of the final MAPbBr$_3$ SCMWAs can be altered by changing the patterns of the templates. For example, using a template with periodic curved-groove microstructures, curved MAPbBr$_3$ SCMWAs were obtained, as shown in Figure 2b. Scanning electron microscopy (SEM) was used to further analyze the morphology of the MAPbBr$_3$ SCMWAs. As shown in Figures 2c,d, the straight and curved arrays, respectively, have a nearly perfect morphology, with a uniform height and width. For the curved microwires in particular, there were no obvious cracks or other defects, even at the turning point (Figure S5, Supporting Information). The enlarged SEM photograph of one single microwire is shown in Figure 2e. As shown in Figure 2f, the transmission electron microscopy (TEM) image further demonstrates the smooth and homogeneous structure of the MAPbBr$_3$ SCMWAs. The sharp and discrete diffraction points in the selected area electron diffraction pattern (insert in Figure 2f) confirm the single crystal characteristics of the MAPbBr$_3$ SCMWAs. Atomic force microscopy (AFM) was also utilized to analyze the surface

**ADVANCED
SCIENCE NEWS**

www.advancedsciencenews.com
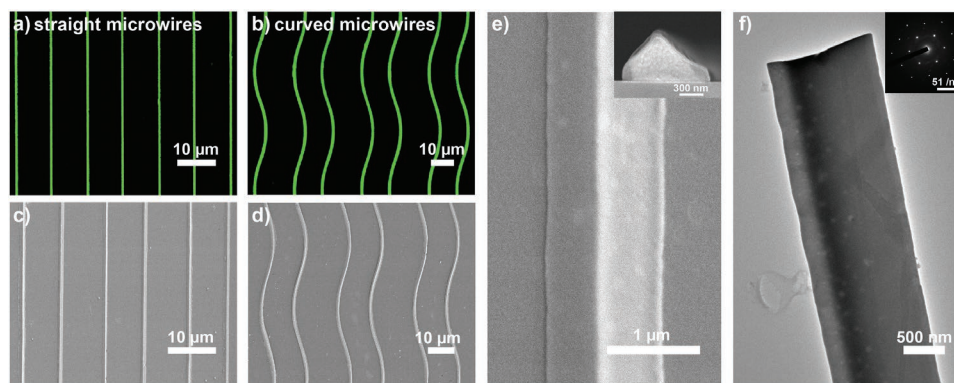
**ADVANCED
MATERIALS**

www.advmat.de
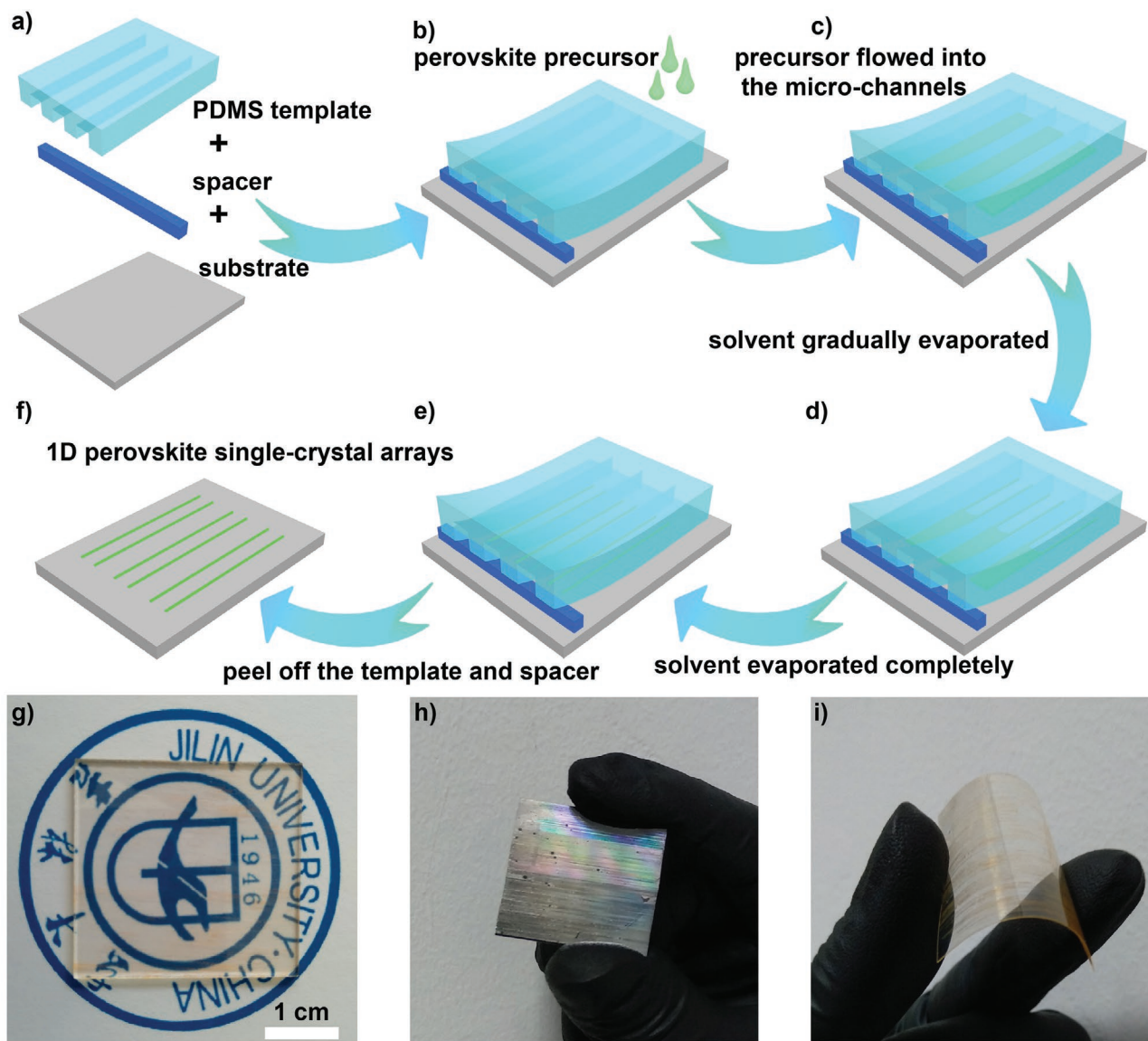
Figure 1. a) Microstructure PDMS film and a spacer were bonded tightly to the substrate to form a series of periodic sealed microchannels. The spacer was used to pad one end of the template to avoid having the PDMS template blown away from the substrate by the vaporized solvent during the solvent evaporation process. b) MAPbBr$_3$ precursor was dropped onto one end of the template. c) Under the guidance of the capillary force, the precursor quickly flowed into these periodic microchannels. d) The solvent gradually evaporated and two liquid tails attached to the sidewalls of each microchannel during the flow of the liquid through the channel. Nucleation and crystallization proceeded along the sidewall of the channel. e) After solvent evaporation, the MAPbBr$_3$ SCMWAs were left on the substrate. f) After the PDMS template and the spacer were peeled off, highly aligned MAPbBr$_3$ SCMWAs were obtained. g–i) Large areas of MAPbBr$_3$ SCMWAs on different substrates: g) glass, h) silicon, and i) PET.

morphology, width, and height of the MAPbBr$_3$ SCMWAs, as shown in Figure S6, Supporting Information. The height and width distributions of the linear and curved arrays are uniform (Figures S6a and S6c, Supporting Information). As shown in the cross-sectional height distribution diagrams in Figure S6b, Supporting Information, different positions along the same crystal are nearly identical, further demonstrating the uniform height and width distribution of the MAPbBr$_3$ SCMWAs. As the energy-dispersive spectroscopy (EDS) mappings show in Figure S7, Supporting Information, Pb and Br are evenly distributed with an atomic ratio of 25.47: 74.53 ≈ 1:3, which

confirms that the MAPbBr$_3$ crystal was successfully prepared. Using fluorescence microscopy, SEM, AFM, TEM, and XRD, the uniform and controllable morphology and good crystallinity of the MAPbBr$_3$ SCMWAs obtained via the proposed method were confirmed.

By altering the PDMS templates, the position, alignment, orientation, pattern, and spacing of the MAPbBr$_3$ SCMWAs can be controlled simultaneously. As shown in Figure S8, Supporting Information, it was possible to fabricate MAPbBr$_3$ SCMWAs with different spacings, ranging from 8 to 245 μm. Notably, ultra-long MAPbBr$_3$ SCMWAs can also be easily fabricated

**ADVANCED
SCIENCE NEWS**

www.advancedsciencenews.com

**ADVANCED
MATERIALS**

www.advmat.de

Figure 2. Characterizations of MAPbBr$_3$ SCMWAs. a,b) Fluorescence images of straight (a) and curved (b) MAPbBr$_3$ SCMWAs excited by a 405 nm laser. c,d) SEM images of straight (c) and curved (d) MAPbBr$_3$ SCMWAs. e) Enlarged SEM image of a MAPbBr$_3$ SCMWA. Insert: cross-sectional SEM image of a MAPbBr$_3$ microwire crystal. f) TEM image of a single MAPbBr$_3$ microwire crystal. Insert picture: selected-area electron diffraction pattern.

utilizing the proposed method. As shown in Figure S9, Supporting Information, a linear microwire array was prepared that was more than 1 mm in length, as well as a curved array that was more than 2 mm in length. These are the longest MAPbBr$_3$ microwire crystals to date, and they may provide numerous advantages for both large-scale industrial production and applications in on-chip integrated devices.

The concentration of the perovskite precursor is a crucial parameter that affects the final size of the SCMWAs. Using a low concentration of the precursor, the height and width of the final microwire are relatively small because of the shortage of perovskite solute. As the concentration increases, the availability of solute leads to an increase in the width and height of the microwires. Therefore, the height and width of the SCMWAs can be regulated by simply adjusting the concentration of the precursor (Figure S10, Supporting Information). The height and width of the MAPbBr$_3$ SCMWAs were 95 and 520 nm, respectively, at a concentration of 5 wt% (Figure S10a, Supporting Information). As the concentration increased to 23.5 wt%, the height and width were able to reach 750 nm and 3.2 µm, respectively, because of the abundance of perovskite solute (Figure S10e, Supporting Information). A series of MAPbBr$_3$ SCMWAs with different heights, ranging from 95 to 750 nm, and widths ranging from 510 nm to 3.2 µm were created by simply adjusting the concentration of the perovskite precursor, ranging from 5 to 23.5 wt%, as shown in Figure S10a–e, Supporting Information. Thus, by simply changing the template and adjusting the concentration of the precursor, MAPbBr$_3$ SCMWAs of a desired pattern and size (including spacing, length, width, and height) can be produced.

The high crystalline quality of the MAPbBr$_3$ SCMWAs is demonstrated by the performance of devices utilizing them. For this study, high-performance photodetectors were prepared using the MAPbBr$_3$ SCMWAs obtained via the proposed method. The photodetector was fabricated by evaporating gold electrodes with a thickness of 200 nm and a gap width of 100 µm onto the MAPbBr$_3$ SCMWAs, as shown in **Figure 3**a. Before basic characterizations of the device, the I–V curve of the device was measured, and the trap density of the MAPbBr$_3$ SCMWAs was calculated, according to the space-charge limited current method. As shown in Figure S11, Supporting Information, the I–V curve exhibits an obvious transition point at V_{TFL} = 2.51 V. The trap density of the MAPbBr$_3$ SCMWAs was calculated to be $n_t = 1.61 \times 10^{11}$ cm^{-3}, using the formula:

$$n_t = 2\varepsilon V_{TFL} / e L^2 \tag{1}$$

where ε is the dielectric constant of MAPbBr$_3$, e is the elemental charge, and L is the gap width. Such a low trap density is attributed to the high crystallization quality of the MAPbBr$_3$ SCMWAs. Under illumination by a 365 nm laser, the electron–hole pairs produced by the light were separated by a bias voltage of 1 V to form the photocurrent. The photoresponse performance of the device, under irradiation from sources of different light intensities, is presented in Figure 3b. The figure shows that the photocurrent had a linear dependence on the intensity of light. As the input power density of the light source was increased from 6.37×10^{-9} to 3.82×10^{-3} W cm^{-2}, the photocurrent increased from 1.86×10^{-11} to 9.50×10^{-7} A. The responsivity of the photodetector, which is often defined by

$$R = (I_p - I_d) / P \tag{2}$$

where I_p and I_d are the photocurrent and dark current, respectively, and P is the input power of the light source, was calculated to be as high as 20 A W^{-1}. The relationship between the current and light intensity, shown in **Figure 4**b, reveals that the device has a wide linear dynamic range (LDR) of 95 dB. The LDR is usually calculated as follows:

$$LDR = 20 \log (I_{max} / I_{min}) \tag{3}$$

where I_{max} and I_{min} represent the upper and lower limits of the photocurrent, respectively. The noise current I_{noise} was analyzed from the noise power density (NPD) spectrum, which was measured by a ProPlus 9812D wafer-level 1/f noise characterization system. As shown in the NPD spectrum in insert picture of Figure 3c, the value of the $I2$ noise was measured from 1 to 100 Hz. The measured LDR value may be an underestimate due to the limited detection range of the ammeter. Therefore, the noise current I_{noise} derived from the NPD spectrum was used as I_{min} to obtain a more accurate LDR value for the

ADVANCED
SCIENCE NEWS
www.advancedsciencenews.com

ADVANCED
MATERIALS
www.advmat.de
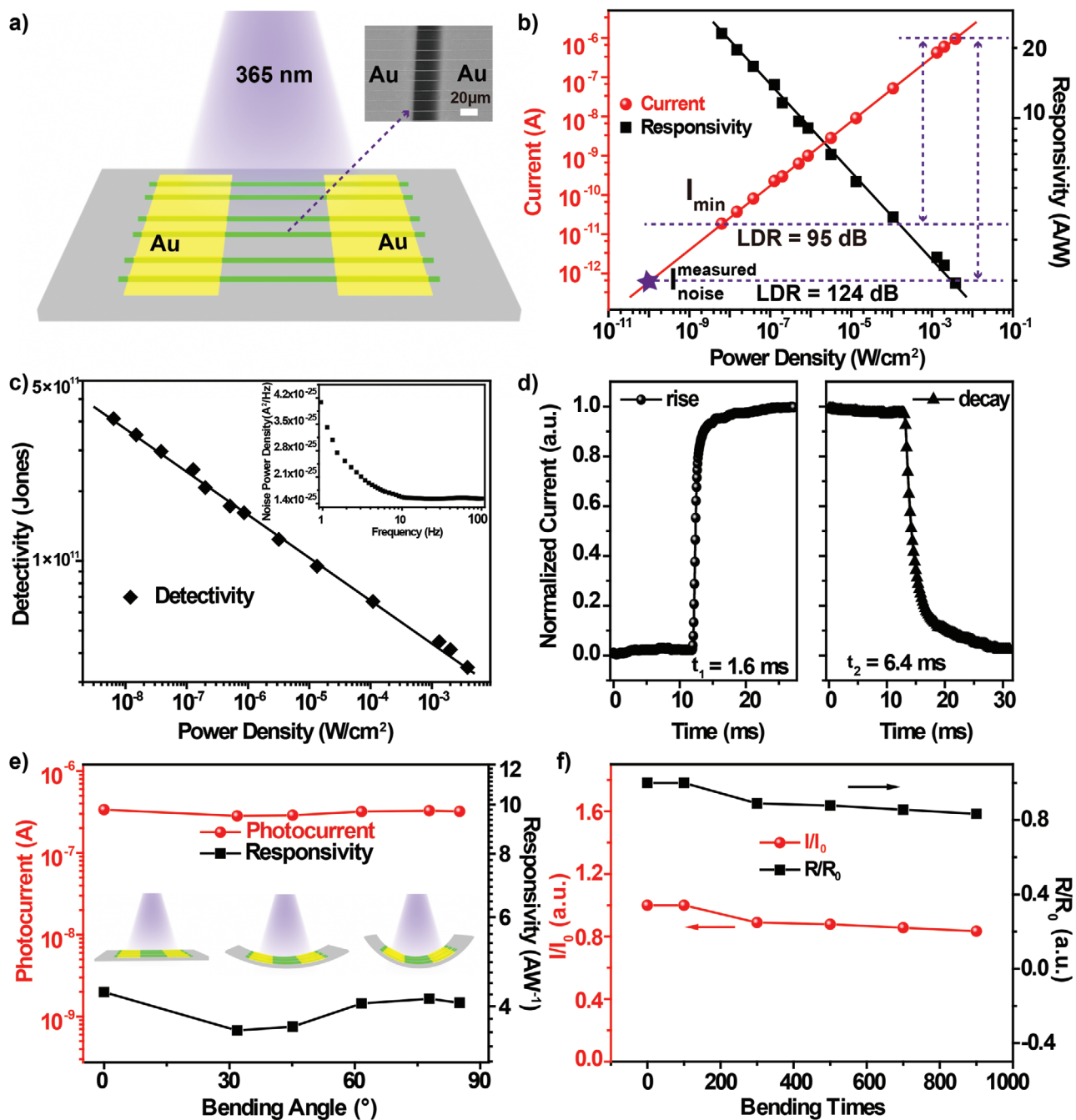
Figure 3. Performance analysis of the photodetector based on the MAPbBr$_3$ SCMWAs on a flat substrate. a) Schematic diagram and SEM image of the photodetector. b) Dependence of the photocurrent and the responsivity of the device on the light intensity, at a bias voltage of 1 V. The device had a high responsivity of 20 A W^{-1} and a wide linear dynamic range of 95 dB. c) The dependence of the detectivity of the device on the light intensity, at a bias voltage of 1 V. Insert: noise power density spectra of the device ranging from 1 to 100 Hz at 1 V bias. d) The response speed of the device was 1.6 ms for rise and 6.4 ms for decay. e) Photocurrent and the responsivity of the device on the inward bending state versus the bending degrees at a bias voltage of 1 V. f) Photocurrent and the responsivity of the device in the bending state versus the bending cycles. The photocurrent and responsivity of the device remained above 80% after 900 bending cycles.

device. Using this calculation, the LDR value obtained was 124 dB, which is comparable to traditional silicon-based photodetectors.[52,53] Noise equivalent power (NEP), an important parameter representing the signal optical power when the

photodetector yields a photocurrent equal to the noise current, is usually calculated according to Equation (4):

$$NEP = I_{noise} / R \qquad (4)$$
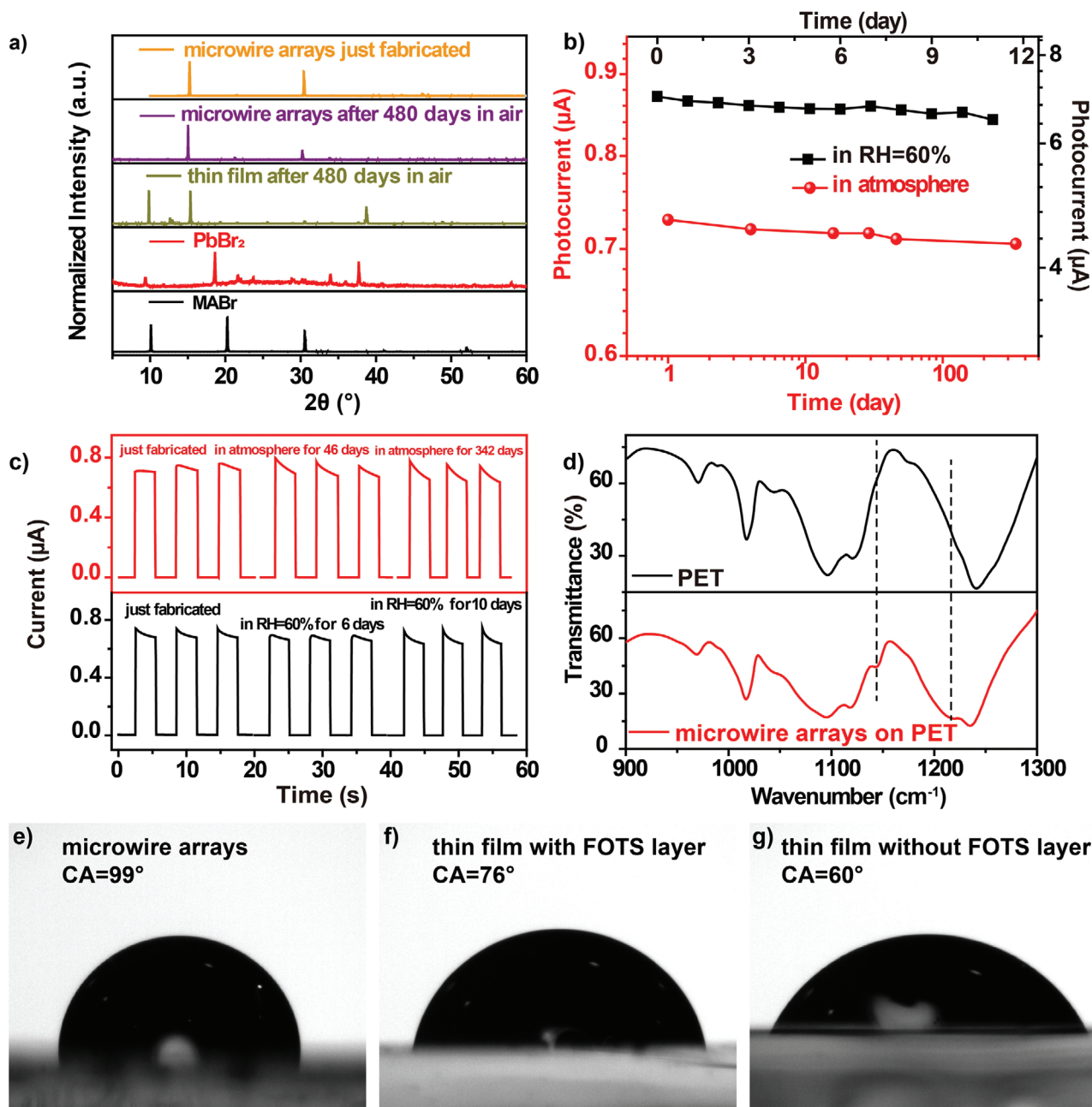
Figure 4. Long-term stability of the device based on MAPbBr$_3$ SCMWAs. a) XRD patterns of the microwires and thin film before and after being exposed to air for 480 d. b) Variation in the photocurrent of the photodetector with exposure time in air and at RH = 60%. After exposure to the air for 342 d, the photocurrent of the device maintained 96.0% of its initial state. c) Response of the device to the pulsed light of the same intensity after 0, 46, and 342 d of exposure in air, and response of the device to the pulsed light of the same intensity after 0, 6, and 10 d of exposure in an environment with a relative humidity of 60%. d) Infrared spectra of the PET and MAPbBr$_3$ SCMWAs prepared on PET substrate. The presence of peaks at 1216 and 1142 cm^{-1} corresponding to the C—F stretching vibrations in the spectra of MAPbBr$_3$ SCMWAs on PET substrate indicates the presence of the FOTS molecules on the surface of MAPbBr$_3$ SCMWAs. e–g) Contact angles of water on three samples: e) sample 1: MAPbBr$_3$ SCMWAs, f) sample 2: MAPbBr$_3$ thin film with FOTS molecules, and g) sample 3: MAPbBr$_3$ thin film without FOTS molecules.

Therefore, the NEP value derived from NPD spectrum was used to calculate the detectivity (D^*), a parameter that characterizes the weakest signal that a photodetector can detect. D^* is often calculated by Equation (5):

$$D^* = \frac{\sqrt{AB}}{\mathrm{NEP}} \tag{5}$$

where A and B represent the active area and the bandwidth, respectively. Figure 3c shows that the photodetector possesses

**ADVANCED
SCIENCE NEWS**

www.advancedsciencenews.com

**ADVANCED
MATERIALS**

www.advmat.de

Table 1. Stability of 1D OIHP-based photodetectors.

Device type	Responsivity [A W^{-1}]	Stability	Maintained performances	Ref.
MAPbBr$_3$ micro/nanowire arrays	20	340 d in air	96%	This work
MAPbI$_3$ networks	0.1	30 d in air	>70%	[56]
MAPbI$_3$ microwire arrays	13.57	>50 d in air		[18]
MAPbI$_3$ microarrays/upconversion nanoparticles	0.27	42 d in 30–40% RH humidity air	70%	[57]
MASnI$_3$ nanowire arrays	0.47	7 d in air	14%	[41]
MAPbI$_3$ nanowire arrays	460	45 d in air		[58]
MAPbI$_3$ nanowires	13.8	90 d in air	90%	[47]
MAPbI$_3$/C8BTBT heterojunction networks	8.1	50 d in air	70%	[59]
PMMA-encapsulated MAPbI$_{3-x}$(SCN)$_x$ nanowires	0.23	21 d in 45–55% RH humidity air	98%	[60]
MAPbI$_3$ nanowires	0.04	60 d in air	12.7%	[61]

a high detectivity up to 4.1×10^{11} Jones. Figure 3d shows the analysis of the response speed of the device. When the device was illuminated, the current increased to the maximum value quickly and remained stable, and the current quickly dropped to its original state when the laser source was turned off. The short response time (1.6 ms for rise and 6.4 ms for decay) proves that the device possesses a fast response speed. The high performance of the photodetector confirms the high crystallization quality of the MAPbBr$_3$ SCMWAs obtained using the proposed method.

The unique geometric structure of the MAPbBr$_3$ SCMWAs endows them with good mechanical properties, which is important for flexible optoelectronic devices. As shown in Figures 3e,f, a flexible photodetector was created based on the MAPbBr$_3$ SCMWAs, using flexible PET as a substrate. The performance of the device while being bent was analyzed. The photocurrent and responsivity of the device did not decrease significantly as the bending angle increased (Figure 3e). The device proved to be superior in durability; the photocurrent and responsivity of the device remained above 80% after 900 bending cycles, as shown in Figure 3f.

Although perovskite materials have superior optoelectronic properties, instability caused by moisture and oxygen is still an obstacle in the application of perovskite-based devices. Grain boundaries and defects in perovskite crystals play an important role in the degradation caused by moisture and oxygen.[38] The decomposition of the perovskite due to oxygen begins at the grain boundary and then extends to the entire crystal.[54] Likewise, moisture-induced perovskite degradation also begins at grain boundaries and advances throughout the crystal.[55] Therefore, the high crystalline quality MAPbBr$_3$ SCMWAs prepared using the proposed method exhibit significantly improved the inherent stability to moisture and oxygen because of lower concentrations of grain boundaries and defects. Figure 4a shows the XRD patterns of the MAPbBr$_3$ SCMWAs and thin film before and after being exposed to the air for 480 d. After exposure to the air for 480 d, the XRD pattern of the MAPbBr$_3$ SCMWAs did not show any obvious new peaks, thus demonstrating its long-term stability. However, noticeable new peaks appeared in the XRD pattern of the MAPbBr$_3$ thin film, which can be attributed to PbBr$_2$. As shown in Figure 4b, the excellent

stability of the MAPbBr$_3$-SCMWA-based photodetector exposed to air and humidity was confirmed. The device maintained 96% of the initial photocurrent value after being exposed to air for more than 340 d, as shown in Figure 4b. The device also had outstanding stability in high humidity environments; even after 10 d of exposure in an environment with a relative humidity of 60%, the device maintained 95% of its initial photocurrent value. Figure 4c shows that the device responded nearly identically to pulsed light of the same intensity after 0, 46, and 342 d of exposure. Similarly, the response of the device to the pulsed light was nearly constant after several days of exposure to the high humidity environment. These results show that the MAPbBr$_3$ SCMWA-based photodetector possesses superior stability. This photodetector is the most stable known 1D OIHP-based photodetector to date (**Table 1**).

Although the high-crystalline-quality perovskite micro/nanowire structures have demonstrated better stability than the thin-film morphology in previous reports, they were far less stable than the MAPbBr$_3$ SCMWAs prepared using the proposed method. In addition to the high crystalline quality, the proposed method of preparation is thought to be an important contribution to the stability of MAPbBr$_3$ SCMWAs. During fabrication of the MAPbBr$_3$ SCMWAs, FOTS molecules on PDMS templates are partially transferred to the surface of the MAPbBr$_3$ SCMWAs and form an in situ encapsulation layer, significantly improving their stability. The presence of the FOTS molecules on the surface of the MAPbBr$_3$ SCMWAs was confirmed through infrared spectroscopy, as shown in Figure 4d. The presence of absorption peaks at 1216 and 1142 cm^{-1} corresponding to the C–F stretching vibrations in the spectra of MAPbBr$_3$ SCMWAs on a PET substrate, indicated that FOTS molecules were successfully transferred onto the surface of the MAPbBr$_3$ SCMWAs during the fabrication process. Moreover, according to the EDS mappings in Figure S12a–c, Supporting Information, the atomic ratio of chlorine and fluorine on the surface of the MAPbBr$_3$ SCMWAs is consistent with that in FOTS, which also confirms the existence of the FOTS protective layer on the surface of the MAPbBr$_3$ SCMWAs. This protective layer is formed in situ during the crystal growth process, so the crystal is protected from the moment it is formed. Therefore, the stability of the MAPbBr$_3$ SCMWAs was significantly enhanced

ADVANCED
SCIENCE NEWS
www.advancedsciencenews.com

ADVANCED
MATERIALS
www.advmat.de

using the method, without any costly and time-consuming post-processing technologies.

Improvements to the microstructure are believed to have the potential to improve the hydrophobicity of the surface of the material.[62] Therefore, the microstructures of highly aligned MAPbBr$_3$ SCMWAs may contribute to improved stability in the presence of moisture. To confirm the contribution of the FOTS molecular layer and microstructure to the improvement of the stability, the contact angles of water were tested on three samples (Figure 4e–g): sample 1, a MAPbBr$_3$ SCMWA; sample 2, a MAPbBr$_3$ film with FOTS molecules; and sample 3, a MAPbBr$_3$ film without FOTS molecules. The contact angle of sample 1 is greater than that of sample 2, indicating that the SCMWAs contribute to the hydrophobicity of the sample. The contact angle of sample 2 is clearly larger than that of sample 3, indicating that the FOTS molecules do improve the resistance of the sample to water. The combination of the protection from the FOTS molecules and the enhancement of the hydrophobicity by the microstructures help ensure the stability of the MAPbBr$_3$ SCMWAs, thereby significantly improving the stability of the devices.

Utilizing the excellent crystallinity and stability of the MAPbBr$_3$ SCMWAs, the application of a MAPbBr$_3$ SCMWAs-based high-performance photodetector was also investigated. As shown in **Figure 5**a and the circuit diagram in Figure S13, Supporting Information, R$_1$ and the photodetector are voltage dividing resistors. When the photodetector is illuminated by the laser source, the current flowing through R$_1$ and the photodetector increases, so that the electric potential of B increases. When the voltage difference between B and E is greater than

0.7 V, the transistor begins to conduct, and the collector current I_C is amplified $I_C \approx \beta I_B$; the amplification factor β is typically ≈100). When the power density of the laser source increased, the resistance of the photodetector decreased, thus the V_1 potential increased. The larger the voltage, the larger I_B is, and the larger I_C becomes. When I_C is larger than the diode's light-emitting current, the LED is turned on, as shown in Figure 5b. When the photodetector is illuminated by a pulsed light, periodic switching of the LED can be achieved. Figure 5c shows the periodic rise and fall of the current, and the corresponding periodic switching of the LED, as shown in Movie S1, Supporting Information. In addition, the switching frequency of the LED can be controlled by controlling the frequency of pulsed light, as shown in Movie S2, Supporting Information. The brightness of the LED can also be adjusted by changing the intensity of the incident light, as shown in Figure 5d and Movie 3, Supporting Information.

In summary, a new method of preparing MAPbBr$_3$ SCMWAs with significantly improved intrinsic stability was proposed. The resistance of the MAPbBr$_3$ SCMWAs prepared using the proposed method to oxygen and moisture was improved in three key aspects: 1) the in situ formed hydrophobic FOTS molecules on the surface of the MAPbBr$_3$ SCMWAs isolate them from water and oxygen, 2) the high crystalline quality ensures that MAPbBr$_3$ SCMWAs have fewer grain boundaries and defects, which play important roles in the degradation process of perovskite induced by oxygen and moisture; and 3) highly ordered microstructures enhance the hydrophobicity of the MAPbBr$_3$ SCMWAs. Therefore, photodetectors based on this perovskite array not only exhibit high performance
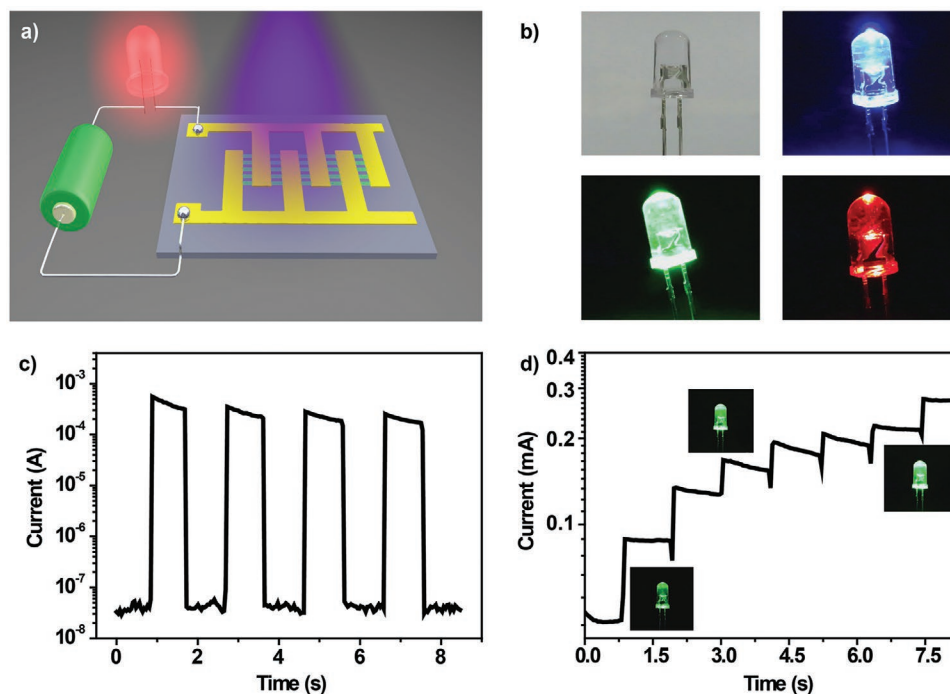
Figure 5. a) The circuit diagram. b) Photograph of the LED in off state and photos of lighted LEDs in red, green, and blue. c) When the photodetector was irradiated by pulsed light, the current raised and fell periodically. d) Different currents under different intensities of light. Insert pictures are photos of LED at different brightness as a result of different intensities of illumination on the photodetector.

(responsivity as high as 20 A W^{-1}, detectivity of as much as 4.1×10^{11} Jones, and I_p/I_d of more than 10^5), but they also show long-term stability (over 1 year exposed to the air and 10 d at a relative humidity of 60%). Additionally, the MAPbBr$_3$ SCMWAs could also be applied in high-performance flexible photodetectors. It is believed that the proposed method may provide a new way to improve the intrinsic stability of a number of different perovskite materials and devices.

Experimental Section

Materials and Preparation of MAPbBr$_3$ Precursor: The photoresist SU8-2025 that was used to prepare silicon templates was purchased from Microchem Inc. PDMS prepolymer and the curing agent were purchased from Dow Corning. MABr and PbBr$_2$ were purchased from Xi'an Polymer Light Technology, Corp., and FOTS was purchased from Sigma Aldrich. All the materials were used without any purification. The MAPbBr$_3$ precursor was prepared by mixing MABr and PbBr$_2$ in DMF at a molar ratio of 1:1, followed by stirring at 60 °C for 12 h.

Template Preparation: First, the photoresist pattern on silicon substrate was obtained by traditional lithography. The obtained silicon templates were silanized by a vacuum process as show in Figure S1, Supporting Information. The silicon templates with line patterns of different widths and 1 μL of FOTS were first sealed in a container. Subsequently, the container was put into a vacuum drier at 40 °C for 8 h to distribute FOTS evenly on the surface of the silicon template. The fabrication procedure of the PDMS template with FOTS on the surface is depicted in Figure S2, Supporting Information. The PDMS prepolymer and the curing agent were mixed at a weight ratio of 10:1. After the bubbles were removed by centrifugation for 10 min, the mixture was spin-coated on the silanized silicon template at a speed of 300 rpm for 30 s. After baking at 95 °C for 90 min, the cured PDMS film was peeled off from the silanized silicon templates with FOTS molecules on it.

Fabrication of MAPbBr$_3$ SCMWAs: After the PDMS was tightly bonded to the substrate, one end of the PDMS template was padded with a small piece of glass to discharge the vaporized solvent. By dropping about 5 μL of precursor at the other end of the PDMS template, under the guidance of the capillary force, the liquid was driven into the microchannels and restricted by the microchannels. The sandwich structure was then placed on a hot plate of 60 °C to accelerate the solvent evaporation and crystallization process. After approximately 10 min, the solvent was completely evaporated and the PDMS template was peeled off, leaving MAPbBr$_3$ SCMWAs on the substrate.

Preparation of Photodetectors Based on MAPbBr$_3$ SCMWAs: Gold film with a thickness of 100 nm was vapor-deposited on both ends of the MAPbBr$_3$ SCMWAs as electrodes, and two silver wires were then pasted onto the electrodes to facilitate the following testing.

Characterization and Photodetector Testing: The morphology and crystallinity of MAPbBr$_3$ SCMWAs were characterized by fluorescence microscopy (Nikon A1RMP, Japan), SEM (JEOL JSM-7500F), AFM (Veeco NanoScope V), TEM (HITACHI Mic-H-600), XRD (Rigaku X-ray, Cu Kα). The *I–V* curves of the device were characterized by Keithley 2600 system under different illumination power densities. The current response of the device under different input light power was recorded by a Keithley 2600 system at a bias voltage of 1 V. A shutter was used to turn a 365 nm laser into a pulse light to test the response of the device to the pulse light, and an oscilloscope (Tektronix) was used to record this response to measure the response time of the device. The noise current of the device was measured by a $1/f$ noise measurement system (Proplu 9812D) at a bias of 1 V from 1 to 100 Hz. The noise current measured at 1 Hz was used as the I_{min} to calculate the LDR. The application of the photodetector experiment was conducted according to the circuit diagram in Figure 5a and Figure S12, Supporting Information. A triode (S8050) was used to amplify the current in the circuit. The resistance values of R_1 and R_B were approximately 10 MΩ and 100 Ω respectively, and the applied voltage was 5 V.

Stability Test: The prepared device was placed in atmosphere and the response of the device was tested at the same intensity of light every few days. Device stability testing in a humidity environment was achieved by placing the device in an environment with a relative humidity of 60%. The environment of RH = 60% was prepared using a saturated sodium bromide solution at room temperature.

Supporting Information

Supporting Information is available from the Wiley Online Library or from the author.

Conflict of Interest

The authors declare no conflict of interest.

[1] C. X. Bao, Z. L. Chen, Y. J. Fang, H. T. Wei, Y. H. Deng, X. Xiao, L. L. Li, J. S. Huang, *Adv. Mater.* **2017**, *29*, 1703209.

[2] Y. J. Fang, C. Bi, D. Wang, J. S. Huang, *ACS Energy Lett.* **2017**, *2*, 782.

[3] S. Y. Shao, J. Liu, G. Portale, H. H. Fang, G. R. Blake, G. H. ten Brink, L. J. A. Koster, M. A. Loi, *Adv. Energy Mater.* **2018**, *8*, 1702019.

[4] C. Xie, P. You, Z. K. Liu, L. Li, F. Yan, *Light: Sci. Appl.* **2017**, *6*, e17023.

[5] Y. J. Fang, Q. F. Dong, Y. C. Shao, Y. B. Yuan, J. S. Huang, *Nat. Photonics* **2015**, *9*, 679.

[6] L. Shen, Y. Fang, J. Huang, in *World Scientific Handbook of Organic Optoelectronic Devices: Perovskite Electronics*, Vol. *1* (Ed: F. So), World Scientific Publishing, Hoboken, NJ, USA **2018**, Ch. 1.

[7] Y. C. Zhao, W. K. Zhou, X. Zhou, K. H. Liu, D. P. Yu, Q. Zhao, *Light: Sci. Appl.* **2017**, *6*, e16243.

[8] L. Lee, J. Baek, K. S. Park, Y. E. Lee, N. K. Shrestha, M. M. Sung, *Nat. Commun.* **2017**, *8*, 15882.

[9] K. Xiao, C. Cui, P. Wang, P. Lin, Y. P. Qiang, L. B. Xu, J. S. Xie, Z. R. Yang, X. D. Zhu, X. G. Yu, D. R. Yang, *Nanotechnology* **2018**, *29*, 065401.

[10] S. B. Kang, J.-H. Kim, M. H. Jeong, A. Sanger, C. U. Kim, C.-M. Kim, K. J. Choi, *Light: Sci. Appl.* **2019**, *8*, 121.

[11] R. Singh, S. R. Suranagi, S. J. Yang, K. Cho, *Nano Energy* **2018**, *51*, 192.

[12] Q. Y. Shang, S. Zhang, Z. Liu, J. Chen, P. F. Yang, C. Li, W. Li, Y. F. Zhang, Q. H. Xiong, X. F. Liu, Q. Zhang, *Nano Lett.* **2018**, *18*, 3335.

[13] X. X. He, P. Liu, S. N. Wu, Q. Liao, J. N. Yao, H. B. Fu, *J. Mater. Chem. C* **2017**, *5*, 12707.

**ADVANCED
SCIENCE NEWS**
www.advancedsciencenews.com

**ADVANCED
MATERIALS**
www.advmat.de

[14] Y. P. Fu, H. M. Zhu, A. W. Schrader, D. Liang, Q. Ding, P. Joshi, L. Hwang, X. Y. Zhu, S. Jin, *Nano Lett.* **2016**, *16*, 1000.

[15] S. Yuan, Z. K. Wang, L. X. Xiao, C. F. Zhang, S. Y. Yang, B. B. Chen, H. T. Ge, Q. S. Tian, Y. Jin, L. S. Liao, *Adv. Mater.* **2019**, *31*, 1904319.

[16] Y. Jin, Z. K. Wang, S. Yuan, Q. Wang, C. C. Qin, K. L. Wang, C. Dong, M. Li, Y. F. Liu, L. S. Liao, *Adv. Funct. Mater.* **2020**, *30*, 1908339.

[17] D. Yin, N. R. Jiang, Y. F. Liu, X. L. Zhang, A. W. Li, J. Feng, H. B. Sun, *Light: Sci. Appl.* **2018**, *7*, 35.

[18] W. Deng, X. J. Zhang, L. M. Huang, X. Z. Xu, L. Wang, J. C. Wang, Q. X. Shang, S. T. Lee, J. S. Jie, *Adv. Mater.* **2016**, *28*, 2201.

[19] S.-X. Li, G.-P. Zhang, H. Xia, Y.-S. Xu, C. Lv, H.-B. Sun, *Nanoscale* **2019**, *11*, 18272.

[20] C. H. Kang, I. Dursun, G. Liu, L. Sinatra, X. Sun, M. Kong, J. Pan, P. Maity, E.-N. Ooi, T. K. Ng, O. F. Mohammed, O. M. Bakr, B. S. Ooi, *Light: Sci. Appl.* **2019**, *8*, 94.

[21] C. L. Li, H. L. Wang, F. Wang, T. F. Li, M. J. Xu, H. Wang, Z. Wang, X. W. Zhan, W. D. Hu, L. Shen, *Light: Sci. Appl.* **2020**, *9*, 31.

[22] X. X. Yin, L. Guan, J. S. Yu, D. W. Zhao, C. L. Wang, N. Shrestha, Y. B. Han, Q. S. An, J. Zhou, B. J. Zhou, Y. Yu, C. R. Grice, R. A. Awni, F. J. Zhang, J. B. Wang, R. J. Ellingson, Y. F. Yan, W. H. Tang, *Nano Energy* **2017**, *40*, 163.

[23] S. Adjokatse, J. Kardula, H. H. Fang, S. Y. Shao, G. H. ten Brink, M. A. Loi, *Adv. Mater. Interfaces* **2019**, *6*, 1801667.

[24] S. Y. Shao, Y. Cui, H. Duim, X. K. Qiu, J. J. Dong, G. H. ten Brink, G. Portale, R. C. Chiechi, S. Q. Zhang, J. H. Hou, M. A. Loi, *Adv. Mater.* **2018**, *30*, 1803703.

[25] W. B. Wang, D. W. Zhao, F. J. Zhang, L. D. Li, M. D. Du, C. L. Wang, Y. Yu, Q. Q. Huang, M. Zhang, L. L. Li, J. L. Miao, Z. Lou, G. Z. Shen, Y. Fang, Y. F. Yan, *Adv. Funct. Mater.* **2017**, *27*, 1703953.

[26] J. L. Miao, F. J. Zhang, *J. Mater. Chem. C* **2019**, *7*, 1741.

[27] L. L. Li, Y. H. Deng, C. X. Bao, Y. J. Fang, H. T. Wei, S. Tang, F. J. Zhang, J. S. Huang, *Adv. Opt. Mater.* **2017**, *5*, 1700672.

[28] L. Shen, Y. J. Fang, D. Wang, Y. Bai, Y. H. Deng, M. M. Wang, Y. F. Lu, J. S. Huang, *Adv. Mater.* **2016**, *28*, 10794.

[29] W. Hu, H. Cong, W. Huang, Y. Huang, L. Chen, A. Pan, C. Xue, *Light: Sci. Appl.* **2019**, *8*, 106.

[30] H. H. Fang, F. Wang, S. Adjokatse, N. Zhao, J. Even, M. A. Loi, *Light: Sci. Appl.* **2016**, *5*, e16056.

[31] X. P. Zheng, Y. H. Deng, B. Chen, H. T. Wei, X. Xiao, Y. J. Fang, Y. Z. Lin, Z. H. Yu, Y. Liu, Q. Wang, J. S. Huang, *Adv. Mater.* **2018**, *30*, 1803428.

[32] Z. L. Chen, C. L. Li, A. A. Zhumekenov, X. P. Zheng, C. Yang, H. Z. Yang, Y. He, B. Turedi, O. F. Mohammed, L. Shen, O. M. Bakr, *Adv. Opt. Mater.* **2019**, *7*, 1900506.

[33] C. L. Li, J. R. Lu, Y. Zhao, L. Y. Sun, G. X. Wang, Y. Ma, S. M. Zhang, J. R. Zhou, L. Shen, W. Huang, *Small* **2019**, *15*, 1903599.

[34] R. Saraf, V. Maheshwari, *ACS Appl. Mater. Interfaces* **2018**, *10*, 21066.

[35] N. Phung, A. Abate, *Small* **2018**, *14*, 1802573.

[36] C. C. Boyd, R. Cheacharoen, T. Leijtens, M. D. McGehee, *Chem. Rev.* **2019**, *119*, 3418.

[37] X. Li, M. I. Dar, C. Yi, J. Luo, M. Tschumi, S. M. Zakeeruddin, M. K. Nazeeruddin, H. Han, M. Grätzel, *Nat. Chem.* **2015**, *7*, 703.

[38] Z. D. Chu, M. J. Yang, P. Schulz, D. Wu, X. Ma, E. Seifert, L. Y. Sun, X. Q. Li, K. Zhu, K. J. Lai, *Nat. Commun.* **2017**, *8*, 2230.

[39] X. Z. Xu, X. J. Zhang, W. Deng, J. S. Jie, X. H. Zhang, *Small Methods* **2018**, *2*, 1700340.

[40] P. H. Wangyang, C. H. Gong, G. F. Rao, K. Hu, X. P. Wang, C. Y. Yan, L. P. Dai, C. Y. Wu, J. Xiong, *Adv. Opt. Mater.* **2018**, *6*, 1701302.

[41] A. Waleed, M. M. Tavakoli, L. Gu, Z. Wang, D. Zhang, A. Manikandan, Q. Zhang, R. Zhang, Y. L. Chueh, Z. Fan, *Nano Lett.* **2017**, *17*, 523.

[42] J. Guo, J. Li, C. Liu, Y. Yin, W. Wang, Z. Ni, Z. Fu, H. Yu, Y. Xu, Y. Shi, Y. Ma, S. Gao, L. Tong, D. Dai, *Light: Sci. Appl.* **2020**, *9*, 29.

[43] H. Deng, D. D. Dong, K. K. Qiao, L. L. Bu, B. Li, D. Yang, H. E. Wang, Y. B. Cheng, Z. X. Zhao, J. Tanga, H. S. Song, *Nanoscale* **2015**, *7*, 4163.

[44] J. Mao, W. E. I. Sha, H. Zhang, X. Ren, J. Zhuang, V. A. L. Roy, K. S. Wong, W. C. H. Choy, *Adv. Funct. Mater.* **2017**, *27*, 1606525.

[45] X. Y. Yang, J. Wu, T. H. Liu, R. Zhu, *Small Methods* **2018**, *2*, 1800110.

[46] M. E. Kamminga, H. H. Fang, M. A. Loi, G. H. Ten Brink, G. R. Blake, T. T. M. Palstra, J. E. Ten Elshof, *ACS Appl. Mater. Interfaces* **2018**, *10*, 12878.

[47] Y. T. Chen, J. Y. Zhang, J. C. Zhou, Y. L. Chu, B. L. Zhou, X. H. Wu, J. Huang, *Adv. Opt. Mater.* **2018**, *6*, 1800469.

[48] F. A. Roghabadi, M. Alidaei, S. M. Mousavi, T. Ashjari, A. S. Tehrani, V. Ahmadi, S. M. Sadrameli, *J. Mater. Chem. A* **2019**, *7*, 5898.

[49] J. G. Feng, X. X. Yan, Y. Liu, H. F. Gao, Y. C. Wu, B. Su, L. Jiang, *Adv. Mater.* **2017**, *29*, 1605993.

[50] W. Wang, Y. Q. Liu, Y. Liu, B. Han, H. Wang, D. D. Han, J. N. Wang, Y. L. Zhang, H. B. Sun, *Adv. Funct. Mater.* **2017**, *27*, 1702946.

[51] J. N. Wang, Y. Q. Liu, Y. L. Zhang, J. Feng, H. Wang, Y. H. Yu, H. B. Sun, *Adv. Funct. Mater.* **2018**, *28*, 1800625.

[52] L. Dou, Y. Yang, J. You, Z. Hong, W.-H. Chang, G. Li, Y. Yang, *Nat. Commun.* **2014**, *5*, 5404.

[53] X. Gong, M. Tong, Y. Xia, W. Cai, J. S. Moon, Y. Cao, G. Yu, C.-L. Shieh, B. Nilsson, A. J. Heeger, *Science* **2009**, *325*, 1665.

[54] Q. Sun, P. Fassl, D. Becker-Koch, A. Bausch, B. Rivkin, S. Bai, P. E. Hopkinson, H. J. Snaith, Y. Vaynzof, *Adv. Energy Mater.* **2017**, *7*, 1700977.

[55] J. A. Christians, P. A. M. Herrera, P. V. Kamat, *J. Am. Chem. Soc.* **2015**, *137*, 1530.

[56] H. Deng, X. K. Yang, D. D. Dong, B. Li, D. Yang, S. J. Yuan, K. K. Qiao, Y. B. Cheng, J. Tang, H. S. Song, *Nano Lett.* **2015**, *15*, 7963.

[57] S. Butler, H. X. Jiang, J. Y. Lin, A. Neogi, *Adv. Opt. Mater.* **2017**, *5*, 1600804.

[58] X. Z. Xu, X. J. Zhang, W. Deng, L. M. Huang, W. Wang, J. S. Jie, X. H. Zhang, *ACS Appl. Mater. Interfaces* **2018**, *10*, 10287.

[59] H. Y. Xia, S. C. Tong, C. J. Zhang, C. H. Wang, J. Sun, J. He, J. Zhang, Y. L. Gao, J. L. Yang, *Appl. Phys. Lett.* **2018**, *112*, 233301.

[60] I. M. Asuo, D. Gedamu, I. Ka, L. F. Gerlein, F. X. Fortier, A. Pignolet, S. G. Cloutier, R. Nechache, *Nano Energy* **2018**, *51*, 324.

[61] S. Li, Y. Li, Z. F. Shi, L. Z. Lei, H. F. Ji, D. Wu, T. T. Xu, X. J. Li, G. T. Du, *Sol. Energy Mater. Sol. Cells* **2019**, *191*, 275.

[62] X. B. Cheng, S. Y. Dong, S. Zhi, S. Paschel, I. Balasa, D. Ristau, Z. S. Wang, *Light: Sci. Appl.* **2019**, *8*, 12.